Universität des Saarlandes

Fachrichtung 6.1 – Mathematik

Enhancing 3-D Cell Structures in Confocal and STED Microscopy: A Joint Model for Interpolation, Deblurring and Anisotropic Smoothing

Nico Persch, Ahmed Elhayek, Martin Welk,
Sven Grewenig, Katharina Narr, Annette Kraegeloh and
Joachim Weickert

Enhancing 3-D Cell Structures in Confocal and STED Microscopy: A Joint Model for Interpolation, Deblurring and Anisotropic Smoothing

Nico Persch

Mathematical Image Analysis Group, Dept. of Mathematics and Computer
Science, Campus E1.7, Saarland University, 66123 Saarbrücken, Germany
persch@mia.uni-saarland.de

Ahmed Elhayek

Max Planck Institute for Computer Science, Dept. 4: Computer Graphics,
Stuhlsatzenhausweg 85, 66123 Saarbrücken, Germany
elhayek@mpi-inf.mpg.de

Martin Welk

University for Health Sciences, Medical Informatics and Technology,
Eduard-Wallnöfer-Zentrum 1, 6060 Hall/Tyrol, Austria
martin.welk@umit.at

Sven Grewenig

Mathematical Image Analysis Group, Dept. of Mathematics and Computer
Science, Campus E1.7, Saarland University, 66123 Saarbrücken, Germany
grewenig@mia.uni-saarland.de

Katharina Narr

INM Leibniz-Institut für Neue Materialien gGmbH, Campus D2.2, Saarland
University, 66123 Saarbrücken, Germany
katharina.narr@inm-gmbh.de

Annette Kraegeloh

INM Leibniz-Institut für Neue Materialien gGmbH, Campus D2.2, Saarland
University, 66123 Saarbrücken, Germany
katharina.narr@inm-gmbh.de

Joachim Weickert

Mathematical Image Analysis Group, Dept. of Mathematics and Computer
Science, Campus E1.7, Saarland University, 66123 Saarbrücken, Germany
weickert@mia.uni-saarland.de

Abstract

This article proposes an advanced image enhancement method that is specifically tailored towards 3-D confocal and STED microscopy imagery. Our approach unifies image denoising, deblurring and interpolation in one joint method to handle the typical weaknesses of these advanced microscopy techniques: Out-of-focus blur, Poisson noise, and low axial resolution. In detail, we propose the combination of (i) Richardson–Lucy deconvolution, (ii) image restoration, and (iii) anisotropic inpainting in one single scheme. To this end, we develop a novel PDE-based model that realises these three ideas. First we consider a basic variational image restoration functional that is turned into a joint interpolation scheme by extending the regularisation domain. Next we integrate the variational representation of Richardson–Lucy deconvolution into our model, and illustrate its relation to Poisson distributed noise. In the following step we supplement the components of our model with subquadratic penalisation strategies, that increase the robustness of the overall method. Finally we consider the associated minimality conditions, where we exchange the occurring scalar-valued diffusivity function by a so-called diffusion tensor. This leads to an anisotropic regularisation that is aligned with structures in the evolving image. As a further contribution of this article, we propose a more efficient and faster semi-implicit iteration scheme that also increases the stability. Our experiments on real data sets demonstrate that this joint model achieves a superior reconstruction quality of the recorded cell.

Keywords: Confocal laser scanning microscopy, stimulated emission depletion microscopy, interpolation, regularisation, deconvolution, Richardson–Lucy, anisotropic diffusion

Contents

1 Introduction

Driven by novel imaging and production techniques, nanotechnology has found its way into modern life in the past years, and is well on track of becoming omnipresent [1, 2]. Since such nano-scale particles are so small that they might penetrate the human body and cells, the natural question about their harmfulness comes up [3, 4, 5], and researchers start examining the possibility of inflammatory or toxicological effects [6].

While the record-breaking lateral resolution of *STimulated Emission Depletion Microscopy (STED)* [7] makes these studies possible, one has to be aware that the underlying image acquisition process has several systematic drawbacks. To understand these limitations, let us briefly discuss this process for the case of confocal microscopy techniques [8].

Standard wide-field microscopes acquire the whole probe at once, whereas in confocal microscopy the specimen is illuminated and scanned point-wisely. To this end, a pinhole and a lens system in front of a light source focus a light beam on one spot of the specimen. In *Confocal Laser Scanning Microscopy (CLSM)* [9], this point illumination is realised by a laser. To block remaining light coming from out-of-focus areas of the lens system, a second pinhole is placed in front of the detector. Often, CLSM is extended by the fluorescence technique [10, 9], where fluorophores are used to label sub-cellular structures in the cell. By adjusting the laser beam to the specific wavelength of the fluorophores, photons of a longer wavelength [10] are emitted. Using a dichroic mirror, only these emitted photons arrive in the detector. Although the CLSM principle allows very high resolutions, the excitation beam cannot be focussed arbitrarily sharp: The size of both the illumination spot and the
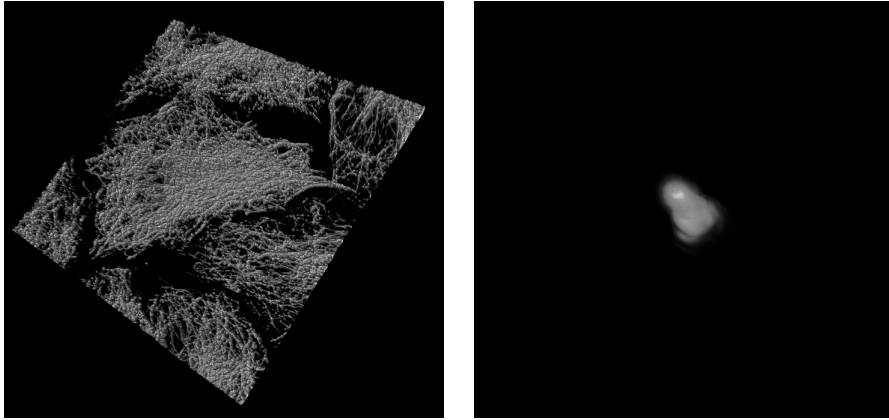
Figure 1: **(a) Left:** Volumetric visualisation of the filament network of a cell, recorded with a 3-D confocal laser scanning microscope (CLSM). **(b) Right:** Scaled point spread function (PSF).

acquisition point is bounded from below by the diffraction law [11]. Thus, the physical resolution limit of CLSM is approximately half the used wavelength. With STimulated Emission and Depletion (STED) microscopy, Hell and Wichmann [7] show a way to break this limitation. By using a second depletion beam, which is doughnut-shaped, already excited molecules can be switched off again. This way, the diffraction law can be bypassed, and a lateral resolution of a few nanometres can be reached. However, it is clear that this idea cannot help to increase the resolution along the depletion beam. Further, due to the two apertures and a second depletion beam, only very few photons finally arrive at the detector. This naturally leads to Poisson distributed noise. By increasing the size of the second pinhole, it is possible to reduce the noise level at the expense of more blur. As a consequence, there exists a natural trade-off between the noise and blur level. The amount of blur, represented by *the point spread function (PSF)* of the device, can be estimated: By aligning and averaging recordings of some small fluorescent beads, software packages like Huygens[6] allow to approximate the PSF within a preprocessing step. A volumetric visualisation[7] of an exemplary 3-D CLSM image together with the estimated PSF is depicted in Figure 1.

Our contribution. Following the considerations above, the STED image acquisition process suffers from three degradations: Poisson noise, a relatively low axial resolution, and out-of-focus blur. The goal of this article is to develop an advanced method to counteract these degradations after the

---

[6]Scientific Volume Imaging b.v., Huygens Software, *http://www.svi.nl*

[7]*http://www.imagevis3d.org*

image has been acquired. This article is based on a conference publication by Elhayek et al. (2011) [12]. Besides revisiting and discussing the latter paper in detail, we extend its model in three aspects:

1. Instead of the isotropic regularisation of [12], we introduce an anisotropic smoothing operator that is well suited for the elongated structures of the cell filament. To accomplish this, the scalar-valued diffusivity is replaced by a tensor-valued quantity, which allows to direct the smoothing along fibres.

2. We propose a novel semi-implicit numerical scheme that is more robust and at the same time faster. More precisely, our scheme allows larger amounts of regularisation and exhibits a significantly faster convergence behaviour than the scheme in [12].

3. We provide extensive numerical experiments that validate the suitability of our modifications. To this end, we evaluate our approach on real world CLSM as well as STED images and compare it against competing methods in literature.

Related work. While van Cittert [13] was one of the first researchers to consider the task of deconvolution, Wiener popularised the discipline with his seminal work [14]. Since then deconvolution has been the topic of numerous publications. Among those, the methods of Richardson [15] and Lucy [16] (RL deconvolution) are closely related to our approach. The work by Dey et al. [17] develops variational models for the RL scheme, and introduces a regularisation component into the process. Earlier variational non-blind deconvolution models with *total variation (TV)* regularisation date back to the work by Marquina and Osher [18], which also fits into the more general model of Osher and Rudin [19]. Furthermore, blind deconvolution models with simultaneous regularisation are proposed by Chan [20] and Yu-Li [21]. The anisotropic diffusion concepts of Weickert [22] have been introduced to deconvolution by Welk et al. [23]. Sawatzki et al. [24, 25] consider primal-dual algorithms to solve regularised RL deconvolution models.
In the context of image interpolation and inpainting [26], a joint model for 2-D image restoration and inpainting is proposed by Chan [27], who even combined inpainting and blind deconvolution in [28].

Organisation. In the following Section 2, we revisit step by step the isotropic model of Elhayek [12]. In Section 3 we present our first contribution and introduce anisotropic smoothing into Elhayek's model. Section 4 is devoted to our novel semi-implicit iterative scheme. The numerical aspects and stability conditions of this scheme are discussed in Section 5. Finally

4

Section 6 presents our experimental evaluation, and we conclude this article with a summary in Section 7.

2 Simultaneous Interpolation and Deconvolution

As already mentioned, we are confronted with image material whose (i) axial resolution (z-direction) is significantly lower than its lateral resolution (x- and y-direction), (ii) which is perturbed by strong noise, and (iii) which suffers from blur. Hence, the goal of this section is to discuss the joint variational model of Elhayek et al. [12], which is appropriate for such image material.

2.1 Variational Denoising and Interpolation

Let $\Omega \subset \mathbb{R}^3$ denote the whole three-dimensional image domain, where the image shall be reconstructed. Further, let $D \subset \Omega$ be the region where measured image data is available. In practice, usually Ω is a cuboid, and D consists of x-y-slices which are equidistantly spaced in z-direction. Assuming that the recorded data $f : D \to \mathbb{R}$ suffers from noise, we approximate a (piecewise) smooth version $u : D \to \mathbb{R}$ of f by minimising the following energy functional on D:

$$E[u] := \int_D \big(\underbrace{(u-f)^2}_{\text{data term}} + \alpha \cdot \underbrace{\Psi(|\boldsymbol{\nabla} u|^2)}_{\text{smoothness term}} \big) \, \mathrm{d}\boldsymbol{x} \ . \tag{1}$$

Here, $\boldsymbol{\nabla} := (\partial_x, \partial_y, \partial_z)^\top$ denotes the gradient operator. The functional (1) consists of a so-called *data term*, which penalises deviations of the solution u from the original data f, and a *smoothness term* whose importance can be tuned via the *regularisation parameter* $\alpha > 0$. Depending on the particular choice of the positive increasing function $\Psi : \mathbb{R}_0^+ \to \mathbb{R}^+$, different smoothing behaviours can be achieved: Choosing $\Psi(s^2) := s^2$ leads to Whittaker-Tikhonov regularisation [29, 30], while $\Psi(s^2) := |s|$ results in total variation (TV) regularisation [31]. It is known that the quadratic data term is especially suitable if the data is perturbed with additive white Gaussian noise. Following [27, 32], we realise the extension to simultaneous denoising and interpolation by simply extending the regularisation domain to the whole cuboid Ω and finding a minimiser $u : \Omega \to \mathbb{R}$ of

$$E[u] := \int_\Omega \big(\chi_D \cdot (u-f)^2 + \alpha \cdot \Psi(|\boldsymbol{\nabla} u|^2) \big) \, \mathrm{d}\boldsymbol{x} \ . \tag{2}$$

5

Here, the characteristic function $\chi_D : \Omega \to \{0, 1\}$ is 1 where information is known (inside D) and 0 everywhere else. Thus, the reconstruction process diffuses information into the unknown regions.

Although this functional realises denoising and interpolation, up to now it does not include a blur model. Moreover, the quadratic data term is inappropriate for Poisson distributed noise, which is the primary noise type in low photon techniques.

2.2 Blur and Noise Model

Confocal microscopy suffers from two main sources of degradation during the imaging process. On the one hand, blur is a big problem due to the imperfectly blocked light from out-of-focus areas. On the other hand, typically the light intensity is so low, that only few photons hit the detector. Hence, strong noise is the result. This problem especially appears in STED microscopy.

To describe these degradations mathematically, let $g : \mathbb{R}^3 \to \mathbb{R}^+$ represent the original image without degradation, and let $f : \mathbb{R}^3 \to \mathbb{R}^+$ denote the acquired image. Since blur is a redistribution of light energy which we assume to be independent of the location, it can be described mathematically in terms of a convolution operation

$$(h * g)(\boldsymbol{x}) := \int_{\mathbb{R}^3} h(\boldsymbol{x} - \boldsymbol{s}) \cdot g(\boldsymbol{s}) \, \mathrm{d}\boldsymbol{s} \tag{3}$$

with the so-called *point spread function (PSF)* $h : \mathbb{R}^3 \to \mathbb{R}^+$. Contrary to blind deconvolution methods [20, 33, 21], in this work we assume the PSF to be known.

Further, we assume also the noise to be a spatially independent function $\eta : \mathbb{R} \to \mathbb{R}$. Thus, the complete image acquisition process can be expressed as

$$f(\boldsymbol{x}) = \eta\left((h * g)(\boldsymbol{x})\right), \quad \boldsymbol{x} \in D. \tag{4}$$

In the typical confocal microscopy setting mainly two different types of noise appear: On the one hand, additive white Gaussian noise, which is independent of the light intensity, is caused by the imaging sensor and by signal amplification. On the other hand, the dominant type of noise in this setting follows a Poisson distribution. Due to the point-wise illumination, the low energy fluorescent light, and the aperture in front of the sensor only a few photons find their way to the detector. The probability of $k \in \mathbb{N}$ photon impacts complies with the Poisson distribution

$$P_\lambda(X = k) = \frac{\lambda^k}{k!} e^{-\lambda} \ , \tag{5}$$

where $\lambda \in \mathbb{R}^+$ is both the mean and the variance of the distribution.

2.3   Richardson–Lucy Deconvolution

According to Dey et al. [17], under the assumption that the photon impacts follow a Poisson distribution, the probability $p(f|g)$ of acquiring the image f, given that the true object is g, reads

$$p(f|g) = \prod_{\boldsymbol{x} \in D} \left(\frac{((h*g)(\boldsymbol{x}))^{f(\boldsymbol{x})}}{f(\boldsymbol{x})!} \; e^{-(h*g)(\boldsymbol{x})} \right) \; . \tag{6}$$

Here we assume that all points $\boldsymbol{x} \in D$ are independent. By a maximum-likelihood approach, the original image g can be estimated as the maximiser of probability p with respect to the observed image f. Hence, by taking the negative logarithm of (6), one obtains the following energy functional [34], whose minimiser u is an approximation to the sought original image g:

$$E_{f,h}^{\mathrm{RL}}[u] := \int_D \left((h*u - f) - f \cdot \ln \left(\frac{h*u}{f} \right) \right) \; \mathrm{d}\boldsymbol{x} \; . \tag{7}$$

Note the equivalence to Csiszár's information divergence [35]. The fact that the latter functional cannot have a unique minimiser is obvious, since any additive perturbation that is removed by convolving with h induces an additional solution.

Concerning the minimisation of (7), the associated minimality condition reads

$$h^* * \left(1 - \frac{f}{h*u} \right) \cdot u = 0 \; . \tag{8}$$

This can be verified by employing the multiplicative Euler-Lagrange formalism (see A). By introducing a fixed point iteration in k, and making use of $h^* * 1 = 1$, where 1 is the constant function 1, we obtain

$$u^{k+1} = \left(h^* * \frac{f}{h*u^k} \right) \cdot u^k \; , \tag{9}$$

where $h^*(\boldsymbol{x}) := h(-\boldsymbol{x})$ is the adjoint of the PSF h. As initialisation for the latter scheme serves the observed image $u^0 := f$, and its only parameter is the number of iterations.

The latter iteration scheme is nothing else than the well known Richardson–Lucy (RL) deconvolution algorithm [16, 15]. It is a common post-processing method in confocal microscopy and astronomical imaging [36] which produces with every iteration successively sharpened images u^k. Note that the minimisation of (7) via the Richardson–Lucy iteration (9) is already proposed

in [17, 34]. In the absence of noise, i.e. $f = h * g$, the undisturbed image g is one fixed point of the RL iteration. However, in practice if noise is present, the scheme has to be stopped after a certain number of iterations since it is known to diverge for $k \to \infty$ [37].

2.4 Robust Regularised Richardson–Lucy Deconvolution

The goal of this section is to combine the regularisation ideas from Section 2.1 with the deconvolution model from the last section.

Hence, analogously to [17, 25, 24, 37], we extend the energy functional (7) with a regularisation term:

$$E_{f,h}^{\mathrm{RRL}}[u] := \int_D \left(\underbrace{h * u - f - f \ln\left(\frac{h * u}{f}\right)}_{\text{deconvolution}} + \alpha \cdot \underbrace{\Psi(|\boldsymbol{\nabla} u|^2)}_{\text{smoothness}} \right) \mathrm{d}\boldsymbol{x} , \quad (10)$$

As for the regularisation functional (1), the amount of regularisation is steered by the parameter α. Besides its denoising effect, the regularisation term also suppresses oscillations and ringing artefacts which are typical for standard deconvolution methods.

Employing the multiplicative Euler-Lagrange framework, the associated minimality condition [37] is stated by the *partial differential equation (PDE)*

$$\left(h^* * \left(1 - \frac{f}{h * u} \right) - \alpha \cdot \operatorname{div}\left(\Psi'(|\boldsymbol{\nabla} u|^2) \, \boldsymbol{\nabla} u \right) \right) \cdot u = 0 . \quad (11)$$

Furthermore, we follow [37], and introduce the concept of robust statistics [38] to the data term. To this end, we apply a non-negative increasing penalisation function $\Phi : \mathbb{R}_0^+ \to \mathbb{R}_0^+$ to the deconvolution expression and obtain the so-called *Robust Regularised Richardson–Lucy (RRRL)* scheme

$$E_{f,h}^{\mathrm{RRRL}}[u] := \int_D \left(\Phi\left(\underbrace{h * u - f - f \ln\left(\frac{h * u}{f}\right)}_{=:r_f(h * u)} \right) + \alpha \cdot \Psi(|\boldsymbol{\nabla} u|^2) \right) \mathrm{d}\boldsymbol{x} . $$

$$(12)$$

By that, we gain robustness against outliers and imprecisions in the deconvolution model, originating e.g. from an incorrectly estimated PSF. We chose $\Phi(s) := 2\sqrt{s + \beta}$ with the small regularisation constant $\beta > 0$. The associated minimality condition is

$$\left(h^* * \left(\Phi'(r_f(h * u)) \left(1 - \frac{f}{h * u} \right) \right) - \alpha \cdot \operatorname{div}(\Psi'(|\boldsymbol{\nabla} u|^2)\boldsymbol{\nabla} u) \right) \cdot u = 0 . $$

$$(13)$$

8

2.5 Joint Variational Approach

To solve both tasks of deconvolution and interpolation, we could apply the methods for interpolation from Section 2.1 and deconvolution from Section 2.4 sequentially. However, as Chan et al. [28] point out, such a naive solution is disadvantageous: Interpolation followed by deconvolution propagates blurred information into missing regions. By reversing the order of application, the support of the PSF overlaps with the unknown areas. Moreover, the acquired data contains information about the signal in the domain to be inpainted due to the convolution that is part of the image acquisition process.

This motivates a joint variational solution as advocated by Chan et al. [28] in the context of blind deconvolution, and by Elhayek et al. [12] in the setting of RRRL deconvolution. There, the following energy functional for *simultaneous interpolation and RRRL deconvolution (IRRRL)* is proposed:

$$E_{f,h}^{\mathrm{IRRRL}}[u] := \int_{\Omega} \left(\chi_D \cdot \Phi \left(h * u - f - f \ln\frac{h * u}{f} \right) + \alpha \cdot \Psi(|\boldsymbol{\nabla} u|^2) \right) \, \mathrm{d}\boldsymbol{x} \, , \tag{14}$$

which performs simultaneous interpolation and deconvolution. The corresponding minimality condition reads

$$\left(h^* * \left(\chi_D \cdot \Phi'(r_f(u * h)) \left(1 - \frac{f}{u * h} \right) \right) - \alpha \cdot \mathrm{div}(\Psi'(|\boldsymbol{\nabla} u|^2)\boldsymbol{\nabla} u) \right) \cdot u = 0 \, . \tag{15}$$

The latter joint variational model forms the basis of our anisotropic regularisation scheme, which is described in the next section.

3 Fibre Enhancement with Anisotropic Regularisation

So far, we have discussed several interpolation and deconvolution models, which all utilise the concept of regularisation in some sense. Mathematically, such smoothness terms, which penalise the derivative of the unknown, cause a divergence expression of type

$$\mathrm{div} \left(\, \Psi'(|\boldsymbol{\nabla} u|^2) \, \boldsymbol{\nabla} u \, \right) \tag{16}$$

in the associated minimality conditions. Such expressions are known to lead to scalar-valued (isotropic) diffusion [39].

However, the aim of this study is the enhancement and reconstruction of tube-like patterns as e.g. the microtubules, which are part of the intracellular

structure of cells. For this particular application, the isotropic behaviour of the latter class of processes is not well suited. Thus, in order to enhance one-dimensional structures in 3-D space, we apply the idea of anisotropic diffusion (see e.g. [22]), which can adapt its smoothing behaviour to local directional information. To this end we replace the scalar-valued diffusivity $\Psi' \in \mathbb{R}$ in (16) by a tensor-valued quantity $\boldsymbol{D} \in \mathbb{R}^{3 \times 3}$ leading to:

$$\operatorname{div}\left(\boldsymbol{D}\,\boldsymbol{\nabla} u\right)\,. \tag{17}$$

In contrast to the scalar diffusivity, which is space-variant but can only treat all directions equally, the so-called diffusion tensor allows to handle different directions differently.

An established method for gathering local directional information is to consider the eigendecomposition of the so-called structure tensor [40]

$$\boldsymbol{J}_\rho(\boldsymbol{\nabla} u_\sigma) := \mathcal{K}_\rho * \left(\boldsymbol{\nabla} u_\sigma \boldsymbol{\nabla} u_\sigma^\top\right)\,, \tag{18}$$

where $u_\sigma := \mathcal{K}_\sigma * u$ abbreviates Gaussian convolution with standard deviation σ, and the outer convolution is applied to all entries of the tensor in the argument. The directional information is contained in the eigenvectors and eigenvalues of this positive semi-definite tensor. The essential idea is that the image value does not vary along a fibre. Hence, we are searching for the direction of lowest contrast, which is given by the eigenvector $\boldsymbol{v_3}$ corresponding to the smallest eigenvalue μ_3 of

$$\boldsymbol{J}_\rho(\boldsymbol{\nabla} u_\sigma) = (\boldsymbol{v}_1|\boldsymbol{v}_2|\boldsymbol{v}_3) \begin{pmatrix} \mu_1 & & \\ & \mu_2 & \\ & & \mu_3 \end{pmatrix} \begin{pmatrix} \boldsymbol{v}_1^\top \\ \boldsymbol{v}_2^\top \\ \boldsymbol{v}_3^\top \end{pmatrix}\,, \tag{19}$$

we consider the diffusion tensor as a function of the structure tensor, that applies diffusivity functions to the eigenvalues of its argument. Consequently, using the decomposition (19), we design the diffusion tensor as

$$\boldsymbol{D}(\boldsymbol{J}_\rho(\boldsymbol{\nabla} u_\sigma)) := (\boldsymbol{v}_1|\boldsymbol{v}_2|\boldsymbol{v}_3) \begin{pmatrix} \Psi'(\mu_1) & & \\ & \Psi'(\mu_2) & \\ & & 1 \end{pmatrix} \begin{pmatrix} \boldsymbol{v}_1^\top \\ \boldsymbol{v}_2^\top \\ \boldsymbol{v}_3^\top \end{pmatrix}\,, \tag{20}$$

where $\Psi'(s^2) = 1/\sqrt{1 + s^2/\lambda^2}$ is the Charbonnier diffusivity function [41]. Setting the third eigenvalue to 1 corresponds to homogeneous diffusion along the eigenvector $\boldsymbol{v}_3$. As reasoned above, this choice is suitable to enhance the tube-like structures of microtubules.

Finally, we replace the diffusivity in (15) accordingly and obtain

$$\left(h^* * \left(\chi_D \cdot \Phi'(r_f(u * h)) \left(1 - \frac{f}{u * h}\right)\right) - \alpha \operatorname{div}\left(\boldsymbol{D}(\boldsymbol{J}_\rho(\boldsymbol{\nabla} u_\sigma))\boldsymbol{\nabla} u\right)\right) \cdot u = 0 \ .$$

(21)

The latter PDE is the central topic in the following two sections, where the issues of how to efficiently solve and discretise the equation are discussed.

4   Fast and Stabilized Iteration Scheme

Computing a solution of (21) is a non-trivial task. For the related isotropic case (11), Dey et al. [17] propose the following fixed point iteration:

$$u^{k+1} - \left(h^* * \frac{f}{h * u^k}\right) \cdot u^k - \alpha \operatorname{div}\left(\Psi'(|\boldsymbol{\nabla} u^k|^2)\boldsymbol{\nabla} u^k\right) \cdot u^{k+1} = 0 \ .$$

(22)

In their scheme, the divergence term is evaluated at the old time step k, but multiplied with u^{k+1}. Solving for u^{k+1} yields

$$u^{k+1} = \frac{u^k}{1 - \alpha \operatorname{div}\left(\Psi'(|\boldsymbol{\nabla} u^k|^2)\boldsymbol{\nabla} u^k\right)} \cdot \left(h^* * \frac{f}{h * u^k}\right) \ .$$

(23)

As one can see, the divergence term is part of the denominator. To prevent singularities and negative values, the amount of regularisation has to be limited by allowing only small values for α.

As a remedy, Welk [37] refrains from strictly multiplying the divergence term in (13) with u^{k+1} from the new time step. Instead, he chooses the old time step u^k, if the divergence term has positive sign. Else, he proposes to multiply with u^{k+1}, to obtain

$$\left(h^* * \Phi'^k_D\right) u^{k+1} - \left(h^* * \left(\Phi'^k_D \cdot \frac{f}{h * u^k}\right)\right) u^k - \alpha \operatorname{div}\left(\Psi'(|\boldsymbol{\nabla} u^k|^2)\boldsymbol{\nabla} u^k\right) u^{k+\nu} = 0 \ .$$

(24)

Here, we use the abbreviation $\Phi'^k_D := \chi_D \cdot \Phi'(r_f(h * u^k))$ and set $\nu := 1$, if the divergence term is negative, and $\nu := 0$ else. Solving for u^{k+1} leads to the iteration scheme

$$u^{k+1} = \frac{h^* * \left(\Phi'^k_D \cdot \frac{f}{h * u^k}\right) + \alpha \left[\operatorname{div}\left(\Psi'(|\boldsymbol{\nabla} u^k|^2)\, \boldsymbol{\nabla} u^k\right)\right]_+}{h^* * \Phi'^k_D - \alpha \left[\operatorname{div}\left(\Psi'(|\boldsymbol{\nabla} u^k|^2)\, \boldsymbol{\nabla} u^k\right)\right]_-} \cdot u^k \ ,$$

(25)

where we adopt the notation $[z]_\pm := \frac{1}{2}(z \pm |z|)$ from [37].

11

Although this case distinction ensures the non-negativity of the overall scheme, our experiments show that it still behaves unsatisfactory when high levels of regularisation are used.

We will now propose a novel fixed point iteration with better stability properties: Instead of evaluating the divergence expression completely at the old time step, we propose a semi-implicit realisation, and decide to multiply with u^k from the old time step at the end. By applying this novel fixed point iteration to (21), also the more general anisotropic model can be written as

$$(h^* * \Phi_D'^k)\, u^{k+1} - \left(h^* * \left(\Phi_D'^k\, \frac{f}{h * u^k}\right)\right) u^k - \alpha \operatorname{div}\left(\boldsymbol{D}(\boldsymbol{J}_\rho(\boldsymbol{\nabla} u_\sigma^k))\, \boldsymbol{\nabla} u^{k+1}\right) u^k = 0 \ .$$
(26)

In each iteration, three convolution operations have to be performed. Since each convolution is computationally expensive, we propose to replace the factor u^k in the first subtrahend by u^{k+1}. This new semi-implicit scheme reduces the number of necessary convolutions per iteration by one, and leads to

$$\left(h^* * \left(\Phi_D'^k \cdot \left(1 - \frac{f}{h * u^k}\right)\right)\right) u^{k+1} - \alpha \operatorname{div}\left(\boldsymbol{D}(\boldsymbol{J}_\rho(\boldsymbol{\nabla} u_\sigma^k))\, \boldsymbol{\nabla} u^{k+1}\right) u^k = 0 \ .$$
(27)

The actual solution of the latter equation is carried out using the steepest descent method, to which end we introduce the relaxation parameter τ:

$$-\left(h^* * \left(\Phi_D'^k \cdot \left(1 - \frac{f}{h * u^k}\right)\right)\right) u^{k+1} + \alpha \operatorname{div}\left(\boldsymbol{D}(\boldsymbol{J}_\rho(\boldsymbol{\nabla} u_\sigma^k))\, \boldsymbol{\nabla} u^{k+1}\right) u^k$$
$$= \frac{u^{k+1} - u^k}{\tau} \ . \quad (28)$$

Of course, this novel semi-implicit method can also be transferred to the original Richardson–Lucy approach just by omitting interpolation and setting $\Phi(s) := s$, $\alpha := 0$ (see B).

In the following section, the discretisation of this fixed point iteration scheme is discussed.

5 Space Discretisation

Let a 3-D cell image be sampled on a regular grid of size $N_x \times N_y \times N_z =: N$ with sampling distances h_x, h_y, h_z in x-, y- and z-direction, respectively. Hence a discrete version of the *Interpolating Robust (An)Isotropic Regularised Richardson–Lucy (AIRRRL)* deconvolution scheme (28) has to fulfil

the following equation in each voxel $(i, j, \ell) \in \{1, \ldots, N_x\} \times \{1, \ldots, N_y\} \times \{1, \ldots, N_z\}$:

$$- \underbrace{\left[h^* * \left(\Phi_D'^k \cdot \left(1 - \frac{f}{h * u^k} \right) \right) \right]_{i,j,\ell}}_{\boldsymbol{D_1}} \cdot u_{i,j,\ell}^{k+1} + \alpha \cdot \underbrace{[\operatorname{div}(\boldsymbol{D}(u^k)\boldsymbol{\nabla} u^{k+1})]_{i,j,\ell}}_{\boldsymbol{A}(\boldsymbol{u}^k)\boldsymbol{u}^{k+1}} \cdot \underbrace{u_{i,j,\ell}^k}_{\boldsymbol{D_2}}$$

$$= \frac{u_{i,j,\ell}^{k+1} - u_{i,j,\ell}^k}{\tau} \quad . \quad (29)$$

Using a single-index notation (e.g. row-major ordering), we arrange 3-D signals $u : \mathbb{R}^3 \to \mathbb{R}$ in vectors $\boldsymbol{u} \in \mathbb{R}^N$. This allows to represent the diffusion term, which is discretised using finite differences, in terms of a matrix-vector multiplication $\boldsymbol{A}(\boldsymbol{u}^k)\boldsymbol{u}^{k+1}$. The diagonal matrices $\boldsymbol{D}_1, \boldsymbol{D}_2 \in \mathbb{R}^{N \times N}$ are used to express the pointwise multiplication. For realising the two convolution operations, we exploit the convolution theorem: Spatial convolution becomes multiplications in the Fourier domain. Consequently, we obtain the following vector-valued scheme:

$$- \left(\boldsymbol{D}_1(\boldsymbol{u}^k) - \alpha \cdot \boldsymbol{D}_2(\boldsymbol{u}^k) \cdot \boldsymbol{A}(\boldsymbol{u}^k) \right) \cdot \boldsymbol{u}^{k+1} = \frac{\boldsymbol{u}^{k+1} - \boldsymbol{u}^k}{\tau} \quad , \quad (30)$$

which leads to a system of equations $\mathcal{B}\boldsymbol{x} = \boldsymbol{b}$ to be solved in every iteration step:

$$\underbrace{\left(\boldsymbol{I} + \tau(\boldsymbol{D}_1(\boldsymbol{u}^k) - \alpha \cdot \boldsymbol{D}_2(\boldsymbol{u}^k) \cdot \boldsymbol{A}(\boldsymbol{u}^k)) \right)}_{\mathcal{B}} \cdot \underbrace{\boldsymbol{u}^{k+1}}_{\boldsymbol{x}} = \underbrace{\boldsymbol{u}^k}_{\boldsymbol{b}} \quad . \quad (31)$$

In every iteration k of this scheme the system (31) has to be solved. To this end, we split $\boldsymbol{A} = \boldsymbol{A}_{\mathrm{diag}} + \boldsymbol{A}_{\mathrm{rest}}$ into diagonal and off-diagonal parts and compute the solution using the Jacobi relaxation method with parameter $\omega > 0$:

$$\boldsymbol{x}^{m+1} = (1 - \omega)\boldsymbol{x}^m + \omega \mathcal{D}^{-1}(\mathcal{T}\boldsymbol{x}^m + \boldsymbol{b}), \quad \boldsymbol{x}^0 = \boldsymbol{u}^k, \quad m = 0, 1, 2, \ldots \quad (32)$$

where

$$\begin{aligned} \mathcal{D} &= \boldsymbol{I} + \tau \cdot \left(\boldsymbol{D}_1(\boldsymbol{u}^k) - \alpha \cdot \boldsymbol{D}_2(\boldsymbol{u}^k) \cdot \boldsymbol{A}_{\mathrm{diag}}(\boldsymbol{u}^k) \right) \quad , \\ \mathcal{T} &= \tau \cdot \alpha \cdot \boldsymbol{D}_2(\boldsymbol{u}^k) \cdot \boldsymbol{A}_{\mathrm{rest}}(\boldsymbol{u}^k) \quad . \end{aligned} \quad (33)$$

It remains to prove that if $\boldsymbol{x}^m$ contains only positive entries, the same holds for $\boldsymbol{x}^{m+1}$:

Let us first consider the factor $\mathcal{D}^{-1}$ in (32). Negative entries in this diagonal matrix can appear for large τ, since $\boldsymbol{D}_1$ can have entries of arbitrary sign.

Hence, we derive the following bound on τ:

$$\forall\, p \in \{1, \dots, N\}: \quad \mathcal{D}_{p,p} > 0$$
$$\Leftrightarrow \left[\boldsymbol{I} + \tau\left(\boldsymbol{D}_1 - \alpha \cdot \boldsymbol{D}_2 \cdot \boldsymbol{A}_{\text{diag}}\right)\right]_{p,p} > 0 \qquad (34)$$
$$\Leftrightarrow \left[\boldsymbol{D}_1 - \alpha \cdot \boldsymbol{D}_2 \cdot \boldsymbol{A}_{\text{diag}}\right]_{p,p} > -\frac{1}{\tau}\,.$$

The latter inequality must hold for all $\alpha > 0$, and since $-\alpha \cdot \boldsymbol{D}_2 \cdot \boldsymbol{A}_{\text{diag}} > 0$ we obtain:

$$\min_p \left[\boldsymbol{D}_1 - \alpha \cdot \boldsymbol{D}_2 \cdot \boldsymbol{A}_{\text{diag}}\right]_{p,p} > \min_p \left[\boldsymbol{D}_1\right]_{p,p} > -\frac{1}{\tau}\,. \qquad (35)$$

At this point we distinguish two cases: If $\min_p[\boldsymbol{D}_1]_{p,p} \geq 0$, the condition is fulfilled for all $\tau > 0$ anyway. Otherwise, the theoretical step size of the gradient descent is restricted by the inequality

$$\tau < \frac{-1}{\min_p[\boldsymbol{D}_1]_{p,p}}\,. \qquad (36)$$

Please note that this bound is necessary to ensure the positivity of the solution.

Next, let us discuss the remaining component of (32) that might become negative: Since the matrix $\mathcal{T}$ contains the off-diagonal entries of the discrete anisotropic diffusion operator $\boldsymbol{A}$, the positivity of the term $\mathcal{T}\boldsymbol{x}^m + \boldsymbol{b}$ cannot be guaranteed. Thus, we have to ensure for all $p \in \{1, \dots, N\}$

$$(1 - \omega)[\boldsymbol{x}^m]_p > -\omega\left[\mathcal{D}^{-1}(\mathcal{T}\boldsymbol{x}^m + \boldsymbol{b})\right]_p\,. \qquad (37)$$

The latter inequality is just critical for voxels, where the right hand side is positive. Hence, the following bound on the relaxation parameter can be established:

$$\omega < \min_p \frac{[\boldsymbol{x}^m]_p}{[\boldsymbol{x}^m]_p - \min\{[\mathcal{D}^{-1}(\mathcal{T}\boldsymbol{x}^m + \boldsymbol{b})]_p, 0\}}\,. \qquad (38)$$

Note that in the isotropic case, the positivity of the off-diagonals of $\boldsymbol{A}$ is guaranteed anyway, so no relaxation is necessary ($\omega = 1$). Furthermore, the latter bound is derived for arbitrarily negative entries in $\boldsymbol{A}$. In practice, we can safely set ω in $[0.9, 1.0]$ without observing any experimental problems in practice.

6 Experiments

Our experiments are carried out with images that are provided by the Nano-Cell Interaction group of the Leibniz Institute for New Materials (INM) in Saarbrücken. We use a 3-D Confocal Laser Scanning Microscopy (CLSM) image as well as a STimulated Emission Depletion (STED) microscopy image of cells. The image of the 3-D confocal microscope has a resolution of $1024 \times 1024 \times 50$ voxels with a grid size of $(6.2/6.2/12.6)$ nm. Correspondingly, a PSF is estimated at a grid size of $(2.5/2.5/12.6)$ nm. Since the PSF must have the same grid size than the reconstruction, we have to resample it accordingly: For doubling the depth resolution and leaving the grid in x and y direction unaltered, we need $(6.2/6.2/6.3)$ nm. Hence, the given PSF must be subsampled in lateral direction and supersampled in axial direction. For the supersampling, we use linear interpolation.

Although all our experiments are performed in 3-D, we depict distinctive 2-D slices of the processed volumes for the sake of a better recognisability. Figure 2 shows one such slice of the original CLSM image, along with two levels of magnification. For the rest of this section, we will discuss our results on the basis of these magnifications, since the fine-scale details are better comparable on high magnification levels.

Our first experiment addresses the stability of the semi-implicit scheme (28) for the interesting case of relatively large α. In the isotropic setting, typical choices for α are in the interval $[0.001, 0.05]$. In Figure 3, we present results for isotropic regularisation and compare our scheme against the one of Elhayek et al. [12]. While the numerical scheme of the latter method exhibits chequerboard-like instabilities with increasing α, we show that our semi-implicit scheme remains stable even for very high regularisation weights.

With our next experiment, we illustrate the behaviour of the anisotropic smoothing strategy. To this end, we superimpose a 2-D image slice with a visualisation of the main smoothing orientation in Figure 4. This visualisation is computed by projecting the 3-D eigenvector of the structure tensor that corresponds to the smallest eigenvalue into the 2-D slice. One can see that our anisotropic strategy yields good estimates for the sought smoothing directions.

In our third experiment, we compare our method with the original Richardson–Lucy and the isotropic regularisation strategy of [12]. To assess the interpolation quality of these techniques, we show in Figure 5 an in-between slice of the data set. For the special case of RL deconvolution, we have to fill-in the missing slice by linear interpolation in advance. Richardson–Lucy deconvolution results in very sharp contrasts after 200 iterations. The main
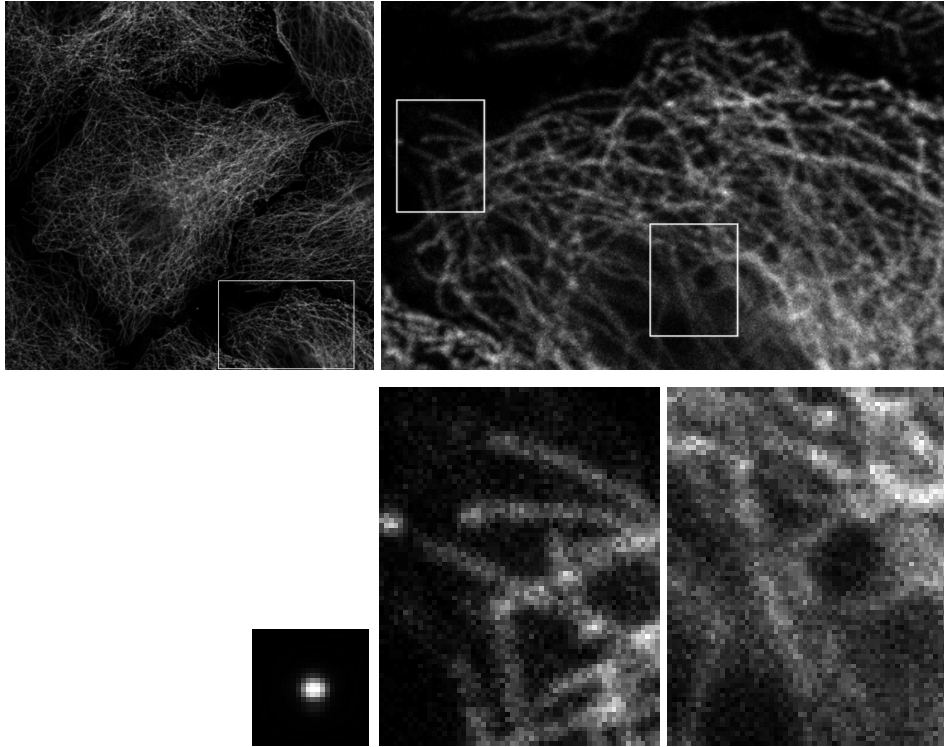
15

Figure 2: Slice 13 of the 3-D CLSM image (grey values rescaled to $[0, 255]$).
(a) Top left: Slice of the complete volume of size $1024 \times 1024 \times 50$. The white rectangle indicates the origin of the first zoom–in. **(b) Top right:** Slice of the volume segment $(376 \times 244 \times 24)$ of (a). Again, the white rectangles show the position of the second level magnifications. **(c) Bottom left:** Central slice of the estimated point spread function (PSF) $(24 \times 24 \times 33)$. Its scale fits the second magnification level. **(d) Bottom centre and (e) right:** Two second-level magnifications.

drawback of the RL algorithm, however, is its sensitivity to noise and the creation of over- and undershoots. As a consequence, the deconvolved images have sharp contrasts, but the fibre structures are inhomogeneous, particularly in crossings. The regularisation component in the methods of Dey et al. and Elhayek et al. suppresses these over- and undershoots. With increasing degree of regularisation, the fibres become more and more smooth and homogeneous. However, at the same time, the radii of single fibres grow and fine structure details melt together, which is shown in Figure 5 (b) and (c). The strength of our anisotropic regularisation becomes obvious by considering Figure 5 (d).

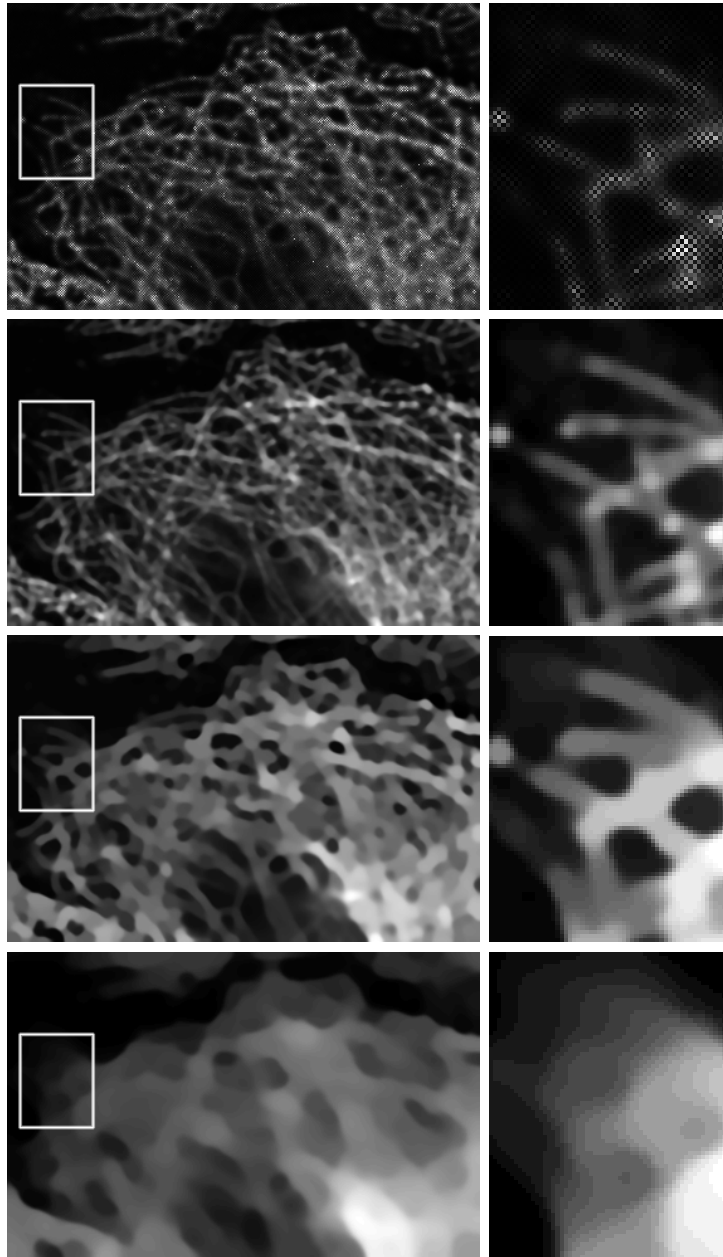Figure 6 documents the suitability of our anisotropic scheme for STED im-

16

Figure 3: Numerical stability with respect to large amount of isotropic regularisations (rescaled to $[0, 255]$). *From Top to Bottom* **(a) Row 1:** Result of the method of Welk and Elhayek et al. 2011 [12, 37], $\alpha = 0.1$, 11 iterations. **(b) Row 2:** Semi-implicit approach with isotropic regularisation $\alpha = 0.1$, 11 iterations. **(c) Row 3:** Same with 900 iterations and $\alpha = 0.1$. **(d) Row 4:** With 900 iterations and $\alpha = 0.5$.
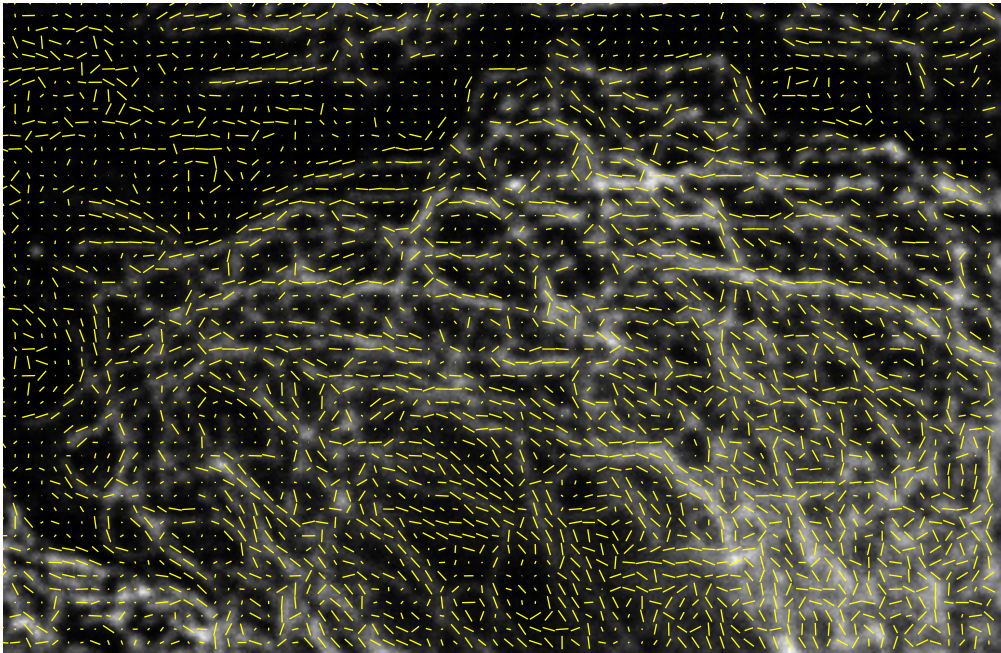
Figure 4: Orientations of the eigenvectors corresponding to the smallest eigenvalues of the structure tensor (19) projected to the actual slice.

ages. The original data of resolution $1057 \times 1059 \times 65$ is acquired with a sampling distance of $(4.0/4.0/16)$ nm. The beads for the PSF estimation are recorded with a sampling distance of $(4.0/4.0/8.4)$ nm, which is already the required grid size for doubling the z-resolution.

The final experiment analyses the runtime of our scheme (28). To show that our novel scheme is significantly faster than the numerical interpolation scheme of Elhayek et al., we compute an approximate steady state using 10,000 iterations of the latter scheme. To reduce the experimentation time, we restrict our computations to a region of size $105 \times 89 \times 47$. In Figure 7 we show the input region along with the approximate solution. Next, we run the scheme of Elhayek et al. as well as our scheme (with a diffusion tensor that realises the same isotropic behaviour) and plot the average difference per voxel between the actual iterate and the approximate solution in Figure 8. One can clearly see the superior convergence rate of our method. Furthermore, we measure the time until the average difference per voxel drops below 0.1 and summarise these computation times in Table 1. All runtime experiments are performed with a C implementation on Intel Xeon Processor W3565 (8M Cache, 3.20 GHz, 4.80 GT/s Intel) CPU with 24 GB RAM using a single-threaded implementation. The upper bound for the relaxation
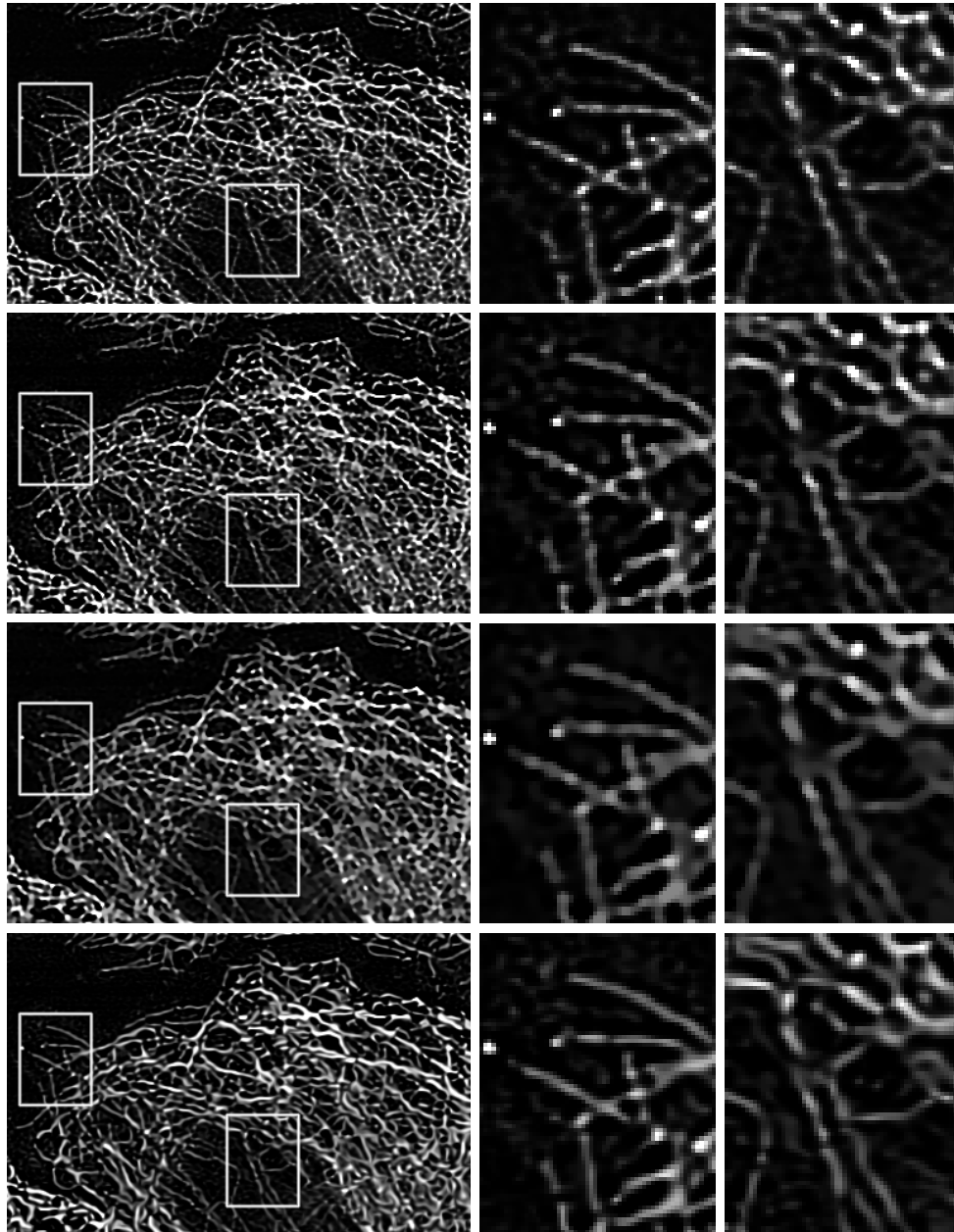
18

Figure 5: Reconstructed slice between slices 13 and 14 of the CLSM cell image (rescaled to $[0, 255]$). *From Top to Bottom* **(a) Row 1:** Richardson–Lucy deconvolution (200 iterations) with preceding linear interpolation. **(b) Row 2:** Isotropic method of Elhayek et al., $\alpha = 0.0006$. **(c) Row 3:** Ditto with $\alpha = 0.002$. **(d) Row 4:** Our anisotropic fibre enhancement method, $\alpha = 0.0004$, $\rho = 1.5$, $\sigma = 0.6$, $\lambda = 0.1$.

Original | Elhayek et al. $\alpha = 0.0004$ | Elhayek, et al. $\alpha = 0.001$

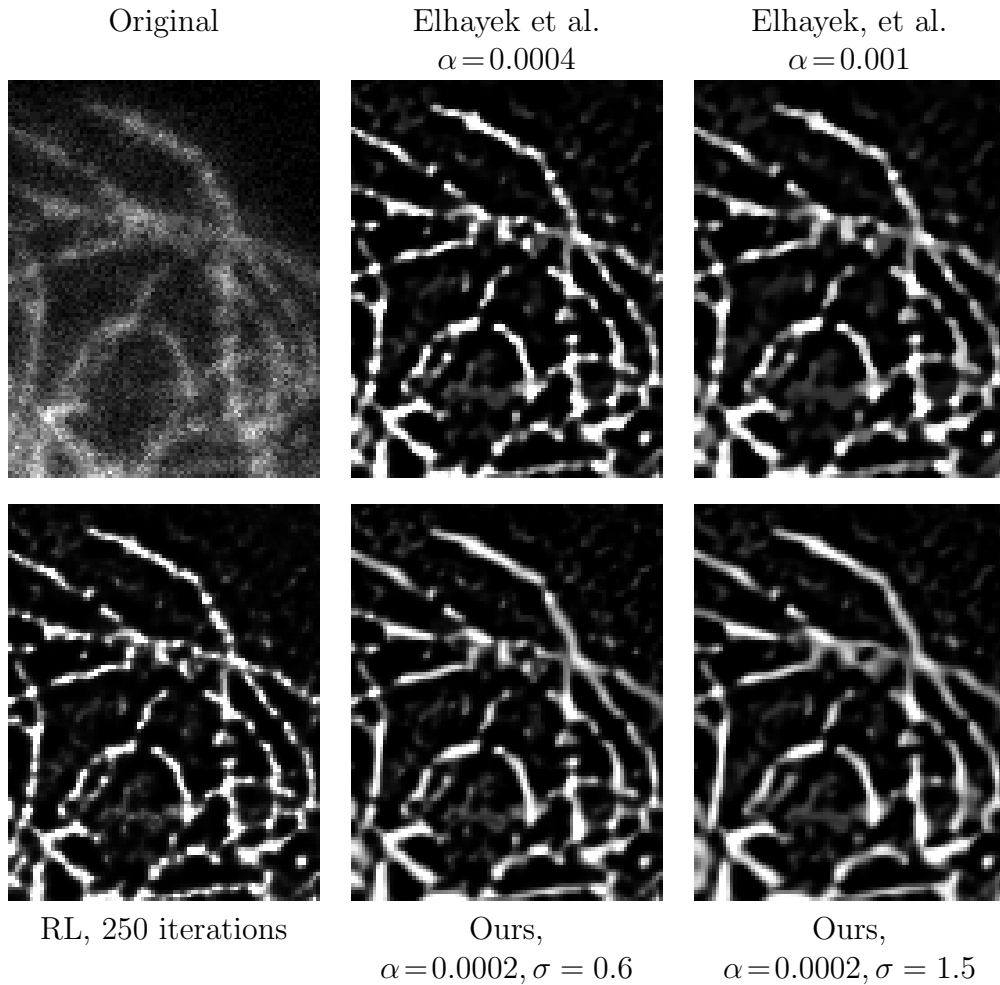RL, 250 iterations | Ours, $\alpha = 0.0002, \sigma = 0.6$ | Ours, $\alpha = 0.0002, \sigma = 1.5$

Figure 6: STED experiment. Reconstruction of cell fibres recorded with a STED microscope. Cut-outs (87×111 px) of an interpolated slice. All images are rescaled to $[0, 255]$. **(a) Top left:** Original input slice. **(b) Top centre:** Result of the method of Elhayek et. al, $\alpha = 0.0004$. **(c) Top right:** Ditto with $\alpha = 0.001$. **(d) Bottom left:** RL deconvolution result after 250 iterations. **(e) Bottom centre:** Our anisotropic scheme from (21), $\alpha = 0.0002$, $\rho = 2.0$, $\sigma = 0.6$, $\lambda = 0.1$. **(f) Bottom right:** Ditto with $\sigma = 1.5$.

parameter $\tau = 1.5$ is determined experimentally. This speed-up can be explained by two facts: On the one hand, the novel semi-implicit scheme only performs two instead of three convolutions per iteration, which leads to a speed-up factor of 1.5. On the other hand, the number of required iterations is decreased by a factor of 2.2.
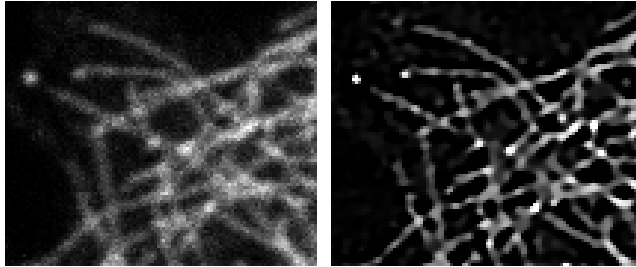
Figure 7: **(a) Left:** Original input CLSM region (rescaled to $[0, 255]$). **(b) Right:** Result after 10,000 iterations using the scheme of Elhayek et al. (2011) with $\alpha = 0.001$.
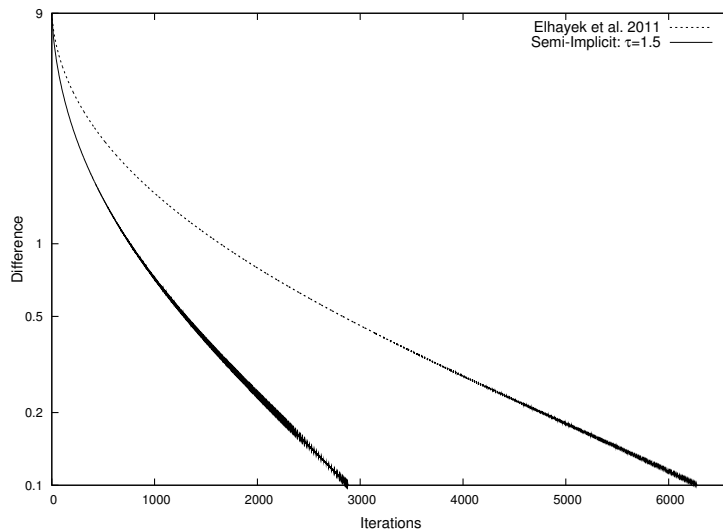

Figure 8: Average L_1 difference between the approximate solution and the iterated signal. Note the logarithmic scaling of the y-axis. **Dotted line:** Elhayek et al. (2011). **Solid line:** Our semi-implicit iteration scheme, $\tau = 1.5$.

Table 1: Computation times of Elhayek et al. and our novel semi-implicit scheme.

Method	Iterations	Time	speed up (time)
Elhayek et al. (2011)	6276	9827 s	1
Semi-implicit $\tau = 1.5$	2879	2982 s	3.3

21

7 Conclusion

We have presented a PDE method for the post-processing and enhancement of modern low photon light microscope imagery arising e.g. in CLSM and STED imaging. The recorded 3-D data typically suffers from blur, Poisson noise and low resolution in the depth direction. To solve these three problems simultaneously, we advocate a combined model that performs deconvolution, denoising, and inpainting. Deconvolution under Poisson noise is taken care of by a Richardson–Lucy term that benefits from additional robustification and regularisation. The regularisation term involves an anisotropic diffusion operator that is also well-suited for inpainting. Moreover, its anisotropy is designed in such a way that it enhances the filament structures of cells. This anisotropic model yields a higher quality of the reconstrution results than its isotropic predecessor from [12]. Moreover, we have discretised our anisotropic model with a novel numerical scheme that preserves the positivity of the solution. Compared to our conference paper [12], it uses explicit and implicit terms in a more powerful way such that its advantages are twofold: It is more stable, and it gains higher efficiency needing less iterations and by saving one out of three convolutions in each iteration step.
Our work shows the benefits of an integrated view on modelling and numerics: Restoring all degradations of the input data simultaneously in a dedicated model guarantees high quality, while an adequate numerical algorithm combines stability and efficiency. We hope that such an integrated view of joint modelling and adequate numerics will become more common in algorithms that support state-of-the-art imaging.

References

[1] BMBF. Nano-initiative action plan. *German Federal Ministry of Education and Research*, 2010.

[2] The Royal Society and The Royal Academy of Engineering. Nanoscience and nanotechnologies: opportunities and uncertainties, 2004.

[3] H. F. Krug and P. Wick. Nanotoxicology: An interdisciplinary challenge. *Angewandte Chemie International Edition*, 50(6):1260–1278, 2011.

[4] N. Lewinski, V. Colvin, and R. Drezek. Cytotoxicity of nanoparticles. *Small*, 4(1):26–49, 2008.

[5] A. Maynard. Nanotechnology: A research strategy for addressing risk. *Woodrow Wilson International Center for Scholars, PEN*, 3, 2006.

[6] I. Weber. Analyse und Modellierung von Fluktuationen intrazellulärer Filamente. Diploma thesis, Department of Theoretical Physics, Saarland University, Saarbrücken, 2010.

[7] S. W. Hell and J. Wichmann. Breaking the diffraction resolution limit by stimulated emission: stimulated-emission-depletion fluorescence microscopy. *Optics Letters*, 19(11):780–782, 1994.

[8] M. Minsky. Memoir on inventing the confocal scanning microscope. *Scanning*, 10:128–138, 1988.

[9] J. B. Pawley, editor. *Handbook of Biological Confocal Microscopy.* Springer, Berlin, 3rd edition, 2006.

[10] J. W. Lichtman and J. A. Conchello. Fluorescence microscopy. *Nature Methods*, 2:910–919, 2005.

[11] E. Abbe. Beiträge zur Theorie des Mikroskops und der Mikroskopischen Wahrnehmung. *Archiv für mikroskopische Anatomie*, Bd. 9, 1873.

[12] A. Elhayek, M. Welk, and J. Weickert. Simultaneous interpolation and deconvolution model for the 3-D reconstruction of cell images. In *Pattern Recognition*, pages 316–325. Springer, Berlin, 2011.

[13] P. H. Cittert. Zum Einfluß der Spaltbreite auf die Intensitätsverteilung in Spektrallinien. II. *Zeitschrift für Physik*, 69:298–308, 1931.

[14] N. Wiener. *Extrapolation, Interpolation, and Smoothing of Stationary Time Series.* MIT Press, Cambridge, 1949.

[15] W. H. Richardson. Bayesian-based iterative method of image restoration. *Journal of the Optical Society of America*, 62:55– 59, 1972.

[16] L. B. Lucy. An iterative technique for rectification of observed distributions. *The Astronomical Journal*, 79(6):745–765, 1974.

[17] N. Dey, L. Blanc-Fraud, C. Zimmer, Z. Kam, P. Roux, J.C. Olivo-Marin, and J. Zerubia. Richardson-Lucy algorithm with total variation regularization for 3D confocal microscope deconvolution. *Microscopy Research Technique*, 69:260–266, April 2006.

[18] A. Marquina and S. Osher. A new time dependent model based on level set motion for nonlinear deblurring and noise removal. In M. Nielsen, P. Johansen, O. F. Olsen, and J. Weickert, editors, *Scale-Space Theories in Computer Vision*, volume 1682 of *Lecture Notes in Computer Science*, pages 429–434. Springer, Berlin, 1999.

[19] S. Osher and L. Rudin. Total variation based image restoration with free local constraints. In *Proc. IEEE International Conference on Image Processing*, pages 31–35, 1994.

[20] T. F. Chan and C. K. Wong. Total variation blind deconvolution. *IEEE Transactions on Image Processing*, 7:370–375, 1998.

[21] Y. You and M. Kaveh. Blind image restoration by anisotropic regularization. *IEEE Transactions on Image Processing*, 8(3):396–407, 1999.

[22] J. Weickert. *Anisotropic Diffusion in Image Processing*. Teubner, Stuttgart, 1998.

[23] M. Welk, D. Theis, T. Brox, and J. Weickert. PDE-based deconvolution with forward-backward diffusivities and diffusion tensors. In R. Kimmel, N. Sochen, and J. Weickert, editors, *Scale Space and PDE Methods in Computer Vision*, volume 3459 of *Lecture Notes in Computer Science*, pages 585–597. Springer, Berlin, 2005.

[24] A. Sawatzky, C. Brune, J. Mueller, and M. Burger. Total variation processing of images with poisson statistics. In X. Jiang and N. Petkov, editors, *Proceedings of the 13th International Conference on Computer Analysis of Images and Patterns*, volume 5702 of *Lecture Notes in Computer Science*, pages 533–540. Springer, July 2009.

[25] A. Sawatzky and M. Burger. Edge-preserving regularization for the deconvolution of biological images in nanoscopy. In G. Psihoyios T. E. Simos and C. Tsitouras, editors, *Proc. 8th International Conference of Numerical Analysis and Applied Mathematics*, volume 1281 of *Conference Proceedings*, pages 1983–1986. AIP, 2010.

[26] M. Bertalmio and G. Sapiro. Image inpainting. In *Proc. ACM SIGGRAPH Conference on Computer Graphics*, pages 417–424, 2000.

[27] T. F. Chan and J. Shen. Mathematical models for local nontexture inpaintings. *SIAM Journal on Applied Mathematics*, 62:1019–1043, 2002.

[28] T. F. Chan, A. M. Yip, and F. E. Park. Simultaneous total variation image inpainting and blind deconvolution. *International Journal of Imaging Systems and Technology*, 15:92–102, 2005.

[29] E. T. Whittaker. A new method of graduation. *Proceedings of the Edinburgh Mathematical Society*, 41:65–75, 1923.

[30] A. N. Tikhonov. Solution of incorrectly formulated problems and the regularization method. *Soviet Mathematics Doklady*, 4:1035–1038, 1963.

[31] L. I. Rudin, S. Osher, and E. Fatemi. Nonlinear total variation based noise removal algorithms. *Physica D*, 60:259–268, 1992.

[32] J. Weickert and M. Welk. Tensor field interpolation with PDEs. In J. Weickert and H. Hagen, editors, *Visualization and Processing of Tensor Fields*, pages 315–325. Springer, Berlin, 2006.

[33] D. A. Fish, A. M. Brinicombe, E. R. Pike, and J. G. Walker. Blind deconvolution by means of the Richardson-Lucy algorithm. *Journal of the Optical Society of America A*, 12(1):58–65, 1995.

[34] D. Snyder, T. J. Schulz, and J. A. O'Sullivan. Deblurring subject to nonnegativity constraints. *IEEE Transactions on Image Processing*, 40(5):1143–1150, 1992.

[35] I. Csiszar. Why least squares and maximum entropy? An axiomatic approach to inference for linear inverse problems. *Annals of Statistics*, 19(4):2032–2066, 1991.

[36] M. Prato, R. Cavicchioli R., L. Zanni, P. Boccacci, and M. Bertero. Efficient deconvolution methods for astronomical imaging: algorithms and IDL-GPU codes. *Astronomy & Astrophysics*, 539:A133, March 2012.

[37] M. Welk. Robust variational approaches to positivity-constrained image deconvolution. Technical Report 261, Department of Mathematics, Saarland University, Saarbrücken, Germany, 2010.

[38] P. J. Huber. *Robust Statistics*, volume 1. Wiley, Chichester, 2004.

[39] P. Perona and J. Malik. Scale space and edge detection using anisotropic diffusion. *IEEE Transactions on Pattern Analysis and Machine Intelligence*, 12:629–639, 1990.

[40] W. Förstner and E. Gülch. A fast operator for detection and precise location of distinct points, corners and centres of circular features. In *Proc. ISPRS Intercommission Conference on Fast Processing of Photogrammetric Data*, pages 281–305, Interlaken, Switzerland, June 1987.

[41] P. Charbonnier, L. Blanc-Féraud, G. Aubert, and M. Barlaud. Deterministic edge-preserving regularization in computed imaging. *IEEE Transactions on Image Processing*, 6(2):298–311, 1997.

[42] T. J. Holmes and Yi-Hwa Liu. Acceleration of maximum-likelihood image restoration for fluorescence microscopy and other noncoherent imagery. *Journal of the Optical Society of America A*, 8(6):893–907, 1991.

A Minimality Conditions of Variational RL Deconvolution

Let us derive the minimality conditions corresponding to the basic energy functional from equation (7). According to [37], we consider the functional

$$E_{f,h}[u] = \int \underbrace{\left(h * u - f - f \cdot \ln \frac{h * u}{f} \right)}_{=r_f(h*u)} \mathrm{d}\boldsymbol{x} \; , \tag{39}$$

and apply the multiplicative Euler-Lagrange formalism as follows: We perturb a minimiser u of $E_{f,h}$ in a multiplicative sense by a test function v, i.e. $u \cdot (1 + \epsilon v)$. Since we obtain the original minimiser for $\epsilon \to 0$, we analyse the derivative of $E_{f,h}$ with respect to ϵ in this point

$$
\begin{aligned}
0 &= \frac{d}{d\epsilon} E_{f,h}[u \cdot (1 + \epsilon v)] \bigg|_{\epsilon=0} \\
&= \frac{d}{d\epsilon} \int \left(h * (u \cdot (1 + \epsilon v)) - f - f \ln \frac{h * (u(1 + \epsilon v))}{f} \right) \mathrm{d}\boldsymbol{x} \bigg|_{\epsilon=0} \\
&= \int \left(\left(1 - \frac{f}{(u \cdot (1 + \epsilon v)) * h} \right) \cdot (uv * h) \right) \mathrm{d}\boldsymbol{x} \bigg|_{\epsilon=0} \\
&= \int \left(\left(1 - \frac{f}{u * h} \right) \cdot (h * uv) \right) \mathrm{d}\boldsymbol{x} \; . \tag{40}
\end{aligned}
$$

Applying the definition of convolution, we obtain

$$\frac{d}{d\epsilon} E_{f,h}[u \cdot (1 + \epsilon v)] \bigg|_{\epsilon=0} = \iint \left(\left(1 - \frac{f}{u * h} \right)(\boldsymbol{x}) \cdot h(\boldsymbol{x} - \boldsymbol{s}) \, u(\boldsymbol{s})v(\boldsymbol{s}) \right) \mathrm{d}\boldsymbol{s} \, \mathrm{d}\boldsymbol{x} \; , \tag{41}$$

and changing the order of integration yields

$$\frac{d}{d\epsilon}E_{f,h}[u(1+\epsilon v)]\bigg|_{\epsilon=0} = \int \left(h^* * \left(1 - \frac{f}{u*h}\right)(\boldsymbol{s}) \cdot u(\boldsymbol{s})v(\boldsymbol{s})\right) \, d\boldsymbol{s} \; . \quad (42)$$

As one can see, this derivative of $E_{f,h}$ evaluates to zero for all test functions v if

$$h^* * \left(1 - \frac{f}{u*h}\right) \cdot u = 0 \; . \quad (43)$$

The latter condition leads to the Richardson–Lucy scheme by introducing the fixed point iteration from Equation (9).

B   A Semi-implicit Relaxation Scheme for RL Deconvolution

The novel semi-implicit iteration scheme can be used to accelerate the standard Richardson–Lucy deconvolution scheme. To this end, we proceed analogously to Section 4, and consider the fixed point iteration (27) for $\Phi_D'^k = 1$ and $\alpha = 0$:

$$\left(h^* * \left(1 - \frac{f}{h*u^k}\right)\right) \cdot u^{k+1} = 0 \; . \quad (44)$$

Applying again the steepest descent method yields

$$-\left(h^* * \left(1 - \frac{f}{h*u^k}\right)\right) \cdot u^{k+1} = \frac{u^{k+1} - u^k}{\tau} \; , \quad (45)$$

which is a semi-implicit version of Holmes' scheme [42]. Finally, we solve for u^{k+1}:

$$u^{k+1} = \left(1 + \tau\left(1 - h^* * \frac{f}{h*u^k}\right)\right)^{-1} \cdot u^k \; . \quad (46)$$

As for the RL scheme (9), if noise is negligible, i.e. $f = h*g$, the undisturbed signal g is a fixed point of the latter scheme. The equivalence for $\Phi_D'^k = 1$, $\alpha = 0$, and $\omega = 1$ also holds in the discrete case (32):

$$\boldsymbol{u}^{k+1} = \left(\mathbf{I} + \tau \cdot \mathbf{D}_1(u^k)\right)^{-1} \cdot \boldsymbol{u}^k \; . \quad (47)$$

The derived condition for τ (36) carries over as well. Compared to the standard Richardson–Lucy scheme, this semi-implicit method requires only about half as many iterations.